Soft orthotropic hyperelastic lattice structures: numerical homogenization and experimental validation

Dror Raf[a], Itay Magen[a], Amit Ashkenazi[a], Lee Jordan[a], Dana Solav[a,*]

[a]*Faculty of Mechanical Engineering, Technion, Haifa, 320003, Israel*

Abstract

Lattice structures have become increasingly popular in various applications due to their lightweight and wide range of effective properties that can be locally tailored by adjusting their geometric features. Finite element (FE) simulations are commonly used to predict their mechanical response and inform inverse design algorithms. However, these simulations pose significant computational demands due to the large number of elements needed for meshing lattice geometries. This challenge can be addressed by replacing lattice geometries with a homogeneous solid of equivalent mechanical properties, a process known as homogenization. However, determining a suitable constitutive model and parameters is difficult, particularly when the response is nonlinear and anisotropic. To this end, this study presents a method for numerically homogenizing orthotropic lattice structures subjected to large elastic deformations. FE simulations of lattice unit cells are employed to quantify their nonlinear elastic response under large uniaxial tension, compression, and simple shear deformations. The simulation results are then used to fit the constitutive model parameters for the effective behavior of the unit cells, employing a Fung orthotropic hyperelastic formulation. The proposed homogenization method is validated through comparisons with full-geometry simulations and compression experiments on beam-based cubic lattice structures manufactured from thermoplastic polyurethane using selective laser sintering. Furthermore, we compare the response of a beam with orthotropic unit cells under bending, which activates multiple deformation modes. The results demonstrate the feasibility and computational efficiency of the proposed homogenization method, highlighting the potential of this approach for efficient modeling and design of lattice structures in engineering applications.

Keywords: Additive manufacturing, digital image correlation (DIC), finite element analysis, metamaterials, multiscale modeling, selective laser sintering (SLS), thermoplastic polyurethane (TPU)

1. Introduction

Additive manufacturing (AM) technologies offer new opportunities to fabricate porous structures with complex shapes and topologies that are difficult or impossible to achieve with conventional manufacturing methods, allowing unprecedented flexibility in design and fabrication

*Corresponding author
Email address: danas@technion.ac.il (Dana Solav)

across various applications and fields [1, 2]. In particular, in the field of biomechanics, AM has opened up possibilities for fabricating data-driven patient-specific devices with locally variable mechanical properties aimed at adjusting the loads transferred to the body through the device. Examples include shoe midsoles [3, 4], insoles [5, 6], prosthetic sockets [7, 8], and wheelchair cushions [9]. By locally adjusting topological and geometrical parameters within the structure, we can tune its macro-scale effective mechanical properties. This allows us to create interfaces with varying properties in different regions, thereby substantially expanding the range of available properties compared to merely combining different solid materials.

The computer-aided design (CAD) of devices like these is typically informed by mechanical numerical simulations, such as the finite element (FE) method, often involving multiple iterations aimed at optimizing the desired mechanical response. However, simulating lattice geometries poses significant computational demands due to the large number of elements needed to mesh them. This problem becomes particularly challenging when a large set of iterative simulations is required in the design process. This challenge can be addressed by replacing the lattice geometry with a homogeneous solid material that has equivalent effective mechanical properties, in a process known as homogenization (e.g., [10, 11, 12]). The goal of this process is to find the parameters of a suitable constitutive law of a solid material, such that it will respond to loads similarly to the lattice structure, as illustrated in the example shown in Figure 1.

To date, most research on 3D-printed lattice structures has primarily focused on lightweight, minimum-compliance structures, which are typically made of relatively stiff materials that exhibit inelastic behavior under large deformations. Consequently, the majority of modeling and simulation studies, as well as commercial CAD tools, have focused their elastic analysis on the linear regime [13, 14, 15, 16, 17, 18].

Recently, there has been increasing interest in the design and fabrication of soft lattice structures and metamaterials that can undergo large (nonlinear) elastic deformations (e.g., [19, 20]). Homogenization of these structures is challenging due to the complexity of constitutive models required to effectively capture their nonlinear response. Some studies limited their analysis to 2D lattice metamaterials or in-plane response (e.g., [10, 21, 22, 23]). Recent advances in the homogenization of 3D lattice structures focused on truss-like structures with slender beams (e.g., [12, 24, 25]). However, although beam elements simplify the simulations and reduce computational costs, they are not applicable to unit cells with thick beams, which are the focus of this study. Moreover, in many cases, the homogenization did not account for both anisotropy and nonlinear elasticity. For example, Jamshidian et al. (2020) [25] presented a multiscale approach using FE simulations with beam elements to evaluate the effective behavior of lattice structures under large uniaxial deformations, focusing on the buckling response, and homogenizing to an isotropic Hyperfoam model. Other studies that homogenized the anisotropic response of lattice structures limited their analysis to the linear elastic regime (e.g., [26, 17]). Shojaee et al. (2024) [27] proposed a homogenization technique for *shell* lattice structures, by fitting their anisotropic linear elastic response using a physics-augmented neural network model. However, a gap remains in establishing a comprehensive framework that captures the full anisotropic and nonlinear elastic behavior of 3D lattice structures with thick-beam unit cells under multiaxial finite deformations.

In this research, we present a method for homogenizing 3D orthotropic lattice structures with thick-beam unit cells that undergo finite deformations in the nonlinear elastic regime. We homogenize their response using the Fung orthotropic hyperelastic constitutive law, considering multiple deformation modes (uniaxial tension, uniaxial compression, and simple shear). We evaluate the accuracy of the method through a comprehensive comparison between the mechan-

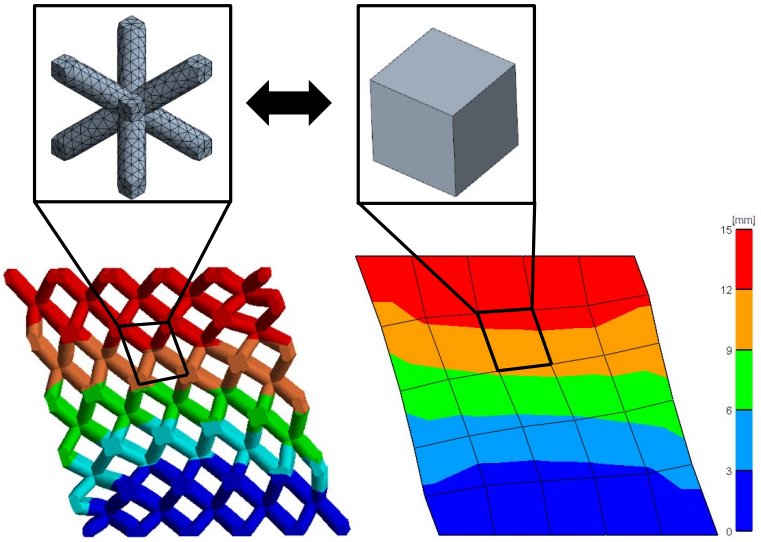

Figure 1: Example of computational homogenization concept: FE simulations of the full lattice structure with numerous elements (left) and of its corresponding homogenized solid model with few elements, exhibiting comparable responses under simple shear, as demonstrated by their horizontal displacements.

ical response (including reaction force and structure deformation) of simulated lattice structures and their homogenized solid counterparts, as well as between FE simulations and experimental results of lattice structures fabricated from thermoplastic polyurethane (TPU) using selective laser sintering (SLS).

2. Materials and Methods

The research methodology integrates experimental testing, FE simulations, and the homogenization framework, organized as follows: subsection 2.1 presents the mechanical characterization of the bulk material, which is used as input for all the full-geometry lattice structure simulations. subsection 2.2 introduces the homogenization procedure and details the periodic boundary conditions (PBCs) in tension, compression, and shear. subsection 2.3 describes the equivalent Fung constitutive model and its model parameters. subsection 2.4 details the FE simulations of unit cells and the process of fitting the Fung model parameters to the simulation results. Then, the experimental methods used to analyze the behavior of body-centered (BC) cubic lattice structures under compression are detailed in subsection 2.5 to 2.8. Then, subsection 2.9 presents the FE simulations corresponding to the experiments, and subsection 2.10 presents a demonstrative FE simulation case of a beam with orthotropic lattice cells under bending, designed to test the homogenization effectiveness when multiple deformation modes are involved. Lastly, subsection 2.11 describes the procedure used to evaluate the accuracy of the homogenized models, considering both reaction forces and 3D structure deformations.

2.1. Characterization of the mechanical properties of the bulk material

The lattice structures used in this research were 3D printed using an SLS printer (Lisa Pro, Sinterit, Warsaw, Poland) from a Flexa Bright™ TPU powder (Sinterit, Warsaw, Poland). In a previous study [28], we characterized the mechanical properties of this material through uniaxial tension and compression tests on specimens printed in multiple orientations. The experiments included pre-conditioning cycles, measurement of stress relaxation, and the estimation of equilibrium force using exponential decay fitting. Full-field strains were measured using 3D digital image correlation (3D-DIC), and micro-CT scans were employed to accurately determine the specimens' cross-sectional areas. The results indicate an approximately linear equilibrium stress-strain relationship up to strains of $\sim \pm 20\%$. However, stiffness varied with printing orientation and between tension and compression. In the current study, we model the material as isotropic linear elastic, a deliberate compromise that balances model fidelity and simplicity. Since different parts in the lattice structures may experience both tension and compression, and are printed in multiple orientations within the same structure, we adopted the average values for the Young's modulus and Poisson ratio obtained from the previous study [28], namely $E = 19.8MPa$ and $\nu = 0.41$, respectively.

2.2. Homogenization with periodic boundary conditions (PBCs)

Periodic boundary conditions (PBCs) are employed to characterize a unit cell's effective mechanical response by applying finite deformations under various loading modes, including uniaxial tension, uniaxial compression, and simple shear, to extract the unit cell's effective homogenized response.

The finite deformation gradient tensor is defined as $\mathbf{F} = \partial\mathbf{x}/\partial\mathbf{X}$, where $\mathbf{X}$ denotes the position vector of a material point in the undeformed (reference) configuration, and $\mathbf{x}$ represents the corresponding position vector in the deformed (current) configuration. For uniaxial tension and compression tests $\mathbf{F}$ takes the form

$$\mathbf{F} = \begin{bmatrix} \lambda_1 & 0 & 0 \\ 0 & \lambda_2 & 0 \\ 0 & 0 & \lambda_3 \end{bmatrix} \tag{1}$$

where $\lambda_1, \lambda_2, \lambda_3$ are the stretches along the axes X,Y,Z respectively. Each stretch is defined as $\lambda_i = 1 + \Delta_i/L_i$, where Δ_i and L_i are the nominal elongation and the initial length of the unit cell in the i^{th} direction, respectively.

For a simple shear test, the deformation gradient tensors are

$$\mathbf{F}_{12} = \begin{bmatrix} 1 & \gamma_{12} & 0 \\ 0 & 1 & 0 \\ 0 & 0 & 1 \end{bmatrix}, \mathbf{F}_{13} = \begin{bmatrix} 1 & 0 & \gamma_{13} \\ 0 & 1 & 0 \\ 0 & 0 & 1 \end{bmatrix}, \mathbf{F}_{32} = \begin{bmatrix} 1 & 0 & 0 \\ 0 & 1 & 0 \\ 0 & \gamma_{32} & 1 \end{bmatrix} \tag{2}$$

where γ_{12}, γ_{13}, and γ_{32} are the nominal shear strains in the shearing planes XY, XZ, and ZY, respectively. The shear strains are defined as $\gamma_{ij} = \Delta_i/L_j$.

For simplicity, the procedure for applying PBCs on a BC unit cell is explained here. This method is applicable to other unit cell types with minor modifications. We consider a generic orthotropic unit cell with three orthogonal symmetry planes that align with the principal axes X,Y,Z. The unit cell is wrapped by a bounding box that represents the equivalent homogenized cell dimensions. The bounding box and the deformation modes on a BC unit cell are shown in Figure 2. We define the nodes of the unit cell that align with the bounding box surfaces as the

outer main nodes, on which we apply the PBCs. There are six sets of outer main nodes, one for each face of the bounding box. The faces of the box will be designated by the unit vector that is normal to each face. The faces U^x, U^y ,U^z and U^{-x} ,U^{-y} ,U^{-z} denote faces associated with the X,Y,Z positive and negative directions, respectively. Each set of outer main nodes has six Degrees of Freedom (DOF), including three translational DOFs and three rotational DOFs. For each node, the transnational DOF U_1, U_2, U_3 denote nodal translation along axis X,Y,Z respectively, and rotational DOF U_4, U_5, U_6 denote nodal rotation about axis X,Y,Z respectively. Therefore, a boundary condition related to the i^{th} face and the j^{th} DOF is denoted as U^i_j.

For each simulation, we define appropriate translational boundary conditions and keep the rotational DOFs unconstrained. For the uniaxial tension and compression tests, we apply zero displacement conditions to U_1^{-x}, U_2^{-y}, and U_3^{-z}. In the direction of the test defined as k (k can be X,Y or Z), we apply displacement Δ_k to U_k^k, and all the transverse directions DOFs are free. For the simple shear test in direction km ($k \neq m$ can be X,Y or Z), we apply zero displacement condition on $U_n^{\pm n}$, where n is the direction orthogonal to the $k-m$ plane. A zero displacement condition is also applied to $U_{k,m}^{-m}$ and U_m^m. A displacement Δ_k is applied to U_k^m.

In order to evaluate the nonlinear response of the lattice structure, we prescribed 10 equally spaced displacement steps. At each displacement step, we record the simulated displacement of the transverse directions and the volume change of the bounding box. Additionally, we compute the simulated volumetric average stress tensor of every element and calculate the volumetric average stress of the simulated model as:

$$\boldsymbol{\sigma}^N_{avg} = \frac{\sum_{i=1}^m v_i \boldsymbol{\sigma}_i}{\sum_{i=1}^m v_i} \tag{3}$$

where m is number of elements in the model, v_i and $\boldsymbol{\sigma_i}$ are the volume and stress of the i^{th} element, and N is the displacement step.

The volume ratio of the unit cell (UC) and the boundary box (BB) is defined by:

$$\beta = \frac{V^N_{UC}}{V^N_{BB}} \tag{4}$$

where $V^N_{BB} = \sum_{i=1}^m v_i$ and $V^N_{UC} = V^0_{UC}\lambda^N_x\lambda^N_y\lambda^N_z$.

Multiplying (3) with (4) yields the stress tensor of the homogenized unit cell:

$$\boldsymbol{\sigma}^N_{BB} = \beta\boldsymbol{\sigma}^N_{avg}\beta \tag{5}$$

2.3. Homogenized constitutive model

To model the large elastic deformations in soft lattice structures, hyperelastic constitutive models are employed to provide closed-form relations between effective stress and deformation. Among the models evaluated, the Fung orthotropic compressible hyperelastic model [29] appeared suitable for capturing both the uniaxial and the shear loading conditions.

The strain energy density (SED) function Ψ for this model can be written as:

$$\Psi = \frac{c_0}{2}\left[e^Q - 1\right] + \frac{\kappa}{2}\left(ln(J)\right)^2 \tag{6}$$

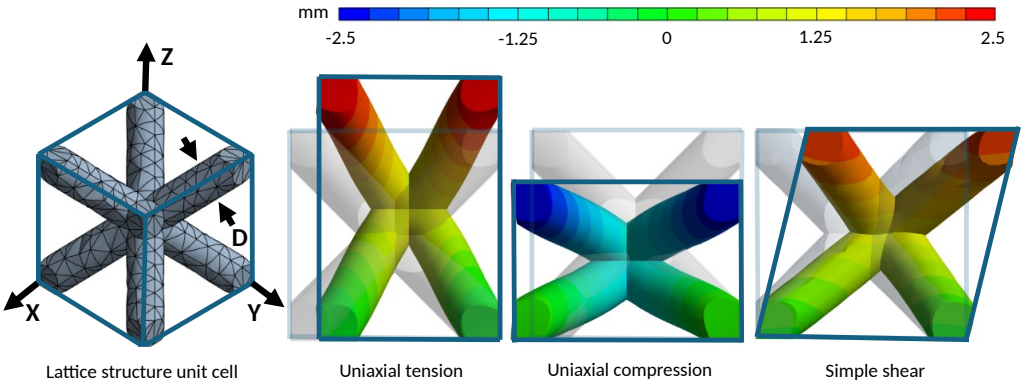

Figure 2: Deformation modes of BC lattice Unit cell. From left to right: The BC unit cell geometry with a beam diameter of D is enclosed by a volume boundary box. Simulation results showing the displacement fields for uniaxial tension and compression (vertical displacement), and simple shear (horizontal displacement).

where the Jacobian $J = det[\mathbf{F}]$ represents the dilatation, and the scalar variable Q for orthotropic symmetries is given by:

$$Q = c_0^{-1} \sum_{i=1}^{3} \left[2\mu_i \mathbf{M}_i : \mathbf{E}^2 + \sum_{j=1}^{3} \lambda_{ij} \left(\mathbf{M}_i : \mathbf{E} \right) \left(\mathbf{M}_j : \mathbf{E} \right) \right] \tag{7}$$

In (7), : denotes a tensorial inner product, the second-order tensor $\mathbf{M}_i$ is defined by $\mathbf{M}_i = \mathbf{V}_i \otimes \mathbf{V}_i$, where $\otimes$ is the outer product and $\mathbf{V}_i$ is the initial direction of material axis i (in the orthotropic case, there are three orthogonal material axes). $\mathbf{E} = (\mathbf{F}^T\mathbf{F} - \mathbf{I})/2$ is the Green-Lagrange strain tensor, where $\mathbf{I}$ is the identity tensor. c_0, κ and the orthotropic Lamé parameters μ_i and λ_{ij} are material parameters. The latter two are related to the Young's moduli E_i, shear moduli G_{ij} and Poisson's ratios ν_{ij} via

$$\begin{bmatrix} \lambda_{11}+2\mu_1 & \lambda_{12} & \lambda_{13} & 0 & 0 & 0 \\ \lambda_{12} & \lambda_{22}+2\mu_2 & \lambda_{23} & 0 & 0 & 0 \\ \lambda_{13} & \lambda_{23} & \lambda_{33}+2\mu_3 & 0 & 0 & 0 \\ 0 & 0 & 0 & \frac{1}{2}(\mu_1+\mu_2) & 0 & 0 \\ 0 & 0 & 0 & 0 & \frac{1}{2}(\mu_2+\mu_3) & 0 \\ 0 & 0 & 0 & 0 & 0 & \frac{1}{2}(\mu_1+\mu_3) \end{bmatrix} =$$

$$= \begin{bmatrix} \frac{1}{E_1} & -\frac{\nu_{12}}{E_1} & -\frac{\nu_{13}}{E_1} & 0 & 0 & 0 \\ -\frac{\nu_{21}}{E_2} & \frac{1}{E_2} & -\frac{\nu_{23}}{E_2} & 0 & 0 & 0 \\ -\frac{\nu_{31}}{E_3} & -\frac{\nu_{32}}{E_3} & \frac{1}{E_3} & 0 & 0 & 0 \\ 0 & 0 & 0 & \frac{1}{G_{12}} & 0 & 0 \\ 0 & 0 & 0 & 0 & \frac{1}{G_{23}} & 0 \\ 0 & 0 & 0 & 0 & 0 & \frac{1}{G_{31}} \end{bmatrix} \tag{8}$$

In case the orthotropic material axes coincide with the X, Y, Z axes, Q is expressed as:

$$
\begin{aligned}
Q = c_0^{-1}(&c_1E_{11}^2 + c_2E_{22}^2 + c_3E_{33}^2 + 2c_4E_{11}E_{22} + 2c_5E_{22}E_{33} + \\
&2c_6E_{23}E_{33} + c_7\left(E_{12}^2 + E_{21}^2\right) + c_8\left(E_{23}^2 + E_{32}^2\right) + c_9\left(E_{31}^2 + E_{13}^2\right))
\end{aligned} \tag{9}
$$

where E_{ij} are components of $\mathbf{E}$ and the material parameters $c_i (i = 1...9)$ are related to the orthotropic Lamé parameters by [30]:

$$
\begin{aligned}
c_1 &= \lambda_{11} + 2\mu_1 \\
c_2 &= \lambda_{22} + 2\mu_2 \\
c_3 &= \lambda_{33} + 2\mu_3 \\
c_4 &= \lambda_{12} \\
c_5 &= \lambda_{23} \\
c_6 &= \lambda_{13} \\
c_7 &= \mu_1 + \mu_2 \\
c_8 &= \mu_2 + \mu_3 \\
c_9 &= \mu_3 + \mu_1
\end{aligned} \tag{10}
$$

Consequently, the Fung model SED yields the Cauchy stress tensor $\boldsymbol{\sigma}$:

$$
\boldsymbol{\sigma} = \frac{c_0}{2}\, J^{-1} e^{Q}\, \mathbf{F}\frac{\partial Q}{\partial \mathbf{E}}\mathbf{F}^{\mathbf{T}} + \kappa\frac{ln(J)}{J} \tag{11}
$$

In the uniaxial case, using (1), (9) and (11) yields the stress components in the principal directions:

$$
\begin{aligned}
\sigma_{11} &= e^{Q}\frac{\lambda_1}{\lambda_2\lambda_3}\left(c_1E_{11} + c_4E_{22} + c_6E_{33}\right) + \kappa\frac{ln(J)}{J} \\
\sigma_{22} &= e^{Q}\frac{\lambda_2}{\lambda_1\lambda_3}\left(c_2E_{22} + c_4E_{11} + c_5E_{33}\right) + \kappa\frac{ln(J)}{J} \\
\sigma_{33} &= e^{Q}\frac{\lambda_3}{\lambda_1\lambda_2}\left(c_3E_{33} + c_5E_{22} + c_6E_{11}\right) + \kappa\frac{ln(J)}{J}
\end{aligned} \tag{12}
$$

In the simple shear case, using (2) , (9) and (11) yields the stresses:

$$
\begin{aligned}
\sigma_{12} &= e^{Q}\left(\frac{c_7\gamma_{12}}{2} + \frac{c_2\gamma_{12}^3}{2}\right) \\
\sigma_{13} &= e^{Q}\left(\frac{c_9\gamma_{13}}{2} + \frac{c_3\gamma_{13}^3}{2}\right) \\
\sigma_{23} &= e^{Q}\left(\frac{c_8\gamma_{23}}{2} + \frac{c_2\gamma_{23}^3}{2}\right)
\end{aligned} \tag{13}
$$

Since the geometry of the selected lattice unit cell has three perpendicular symmetry planes, the mechanical response of the structures is orthotropic. If all three planes are identical, the anisotropy model is reduced to cubic.

2.4. Homogenization simulation framework

The unit cells were modeled using the Lattice feature in Creo Parametric 8.0 (PTC, Inc., Boston, MA, USA), using a "star" configuration composed of beams with a circular cross-section, without corner fillets, as shown in Figure 2. Four BC cubic unit cells of size $10 \times 10 \times 10\,\mathrm{mm}^3$ each were designed with different beam diameter (D): 2.2 *mm*, 2.5 *mm*, 2.8 *mm*, 3.1 *mm*, as well as one BC orthotropic unit cell of size $15 \times 20 \times 17\,\mathrm{mm}^3$ in the X, Y, and Z directions, respectively, and a uniform beam diameter $D = 3.5$ *mm*.

FE simulations of the unit cells were conducted using ANSYS Mechanical 2023 R2 (ANSYS, Inc., Canonsburg, PA, USA). The bulk material parameters were set to an isotropic linear elastic model with the parameters estimated for the Flexa Bright™ TPU, as described in subsection 2.1. The unit cells were meshed with quadratic 20-node hexahedral elements (type SOLID186 in Ansys). A mesh convergence study was conducted to select a mesh that balances between accuracy and computational time. The boundary conditions were employed as described in subsection 2.2. Stress–stretch data obtained from the lattice unit cell simulations were used to determine the parameters of the Fung constitutive model by numerically solving the nonlinear sets of equations (12) and (13), as described in subsection 2.3. A custom MATLAB R2024a code (The Mathworks Inc., Natick, MA, USA), using the *lsqcurvefit* function, was employed to estimate the optimal set of parameters that minimize the least-squares error between the model predictions and the simulation data. Each unit cell was subjected to uniaxial tension-compression stretch (λ), and simple shear strain (γ). For BC cubic cells, we used $\lambda \in [0.8, 1.2]$ and $\gamma \in [0, 0.2]$, whereas for orthotropic cell the deformation ranges were $\lambda \in [0.8, 1.4]$ and $\gamma \in [0, 0.3]$.

2.5. Compression experiments on cubic lattice structures

Four lattice structures composed of 5×5×5 BC cubic unit cells with different beam diameters (D), as described in subsection 2.4, were designed. To the structures designed for fabrication, we added top and bottom solid plates of size $50 \times 5 \times 50\,\mathrm{mm}^3$ in the X, Y, and Z directions, respectively, each with a circular protrusion in the center, as shown in Figure 3a. The structures were processed with Sinterit Studio Advance printing slicer software (Sinterit, Warsaw, Poland). The same default printing parameters used for the TPU characterization experiments (subsection 2.1), including a layer height of 0.1 mm, were employed to generate the g-code for the printer. The structures were printed with the beam axes tilted 45° relative to the printing direction to minimize the variation in the beam dimensions within each lattice structure, as shown in Figure 3a.

The experiments were performed using a horizontal planar biaxial testing system (ADMET, Inc., Norwood, MA, USA) with a 2 kN load cell. The flat ends of the solid plates were glued to aluminum adapters that had a small circular recess to align with the circular protrusion of the structures on one side, and a circular recess to which the compression platens attach on the other side. The experimental setup configuration is shown in Figure 3c.

Since the bulk material exhibited softening during conditioning, a behavior commonly known as Mullin's effect [31], we pre-conditioned the lattice structures by performing 10 cycles of 5 mm displacement compression on each side at a displacement rate of 0.25 mm/s, after which the force-displacement curve became stable. Next, we performed the compression tests with five equally spaced displacement steps. At each displacement step, the test was paused for 400 s, to allow for stress relaxation to occur and collect data for estimating the equilibrium force, as explained in subsection 2.7. During the pause in displacement, force measurements were taken every 1 s. The dimensions of the samples were measured before and after pre-conditioning, as well as before and after the tests, to assess whether any plastic deformations occurred.

2.6. Measurement of lattice structures beam diameter

Due to deviations in geometry between the CAD and printed structures, it was important to assess the actual dimensions of the printed lattice in order to construct FE simulations with the same dimensions. The density of the printed material was estimated by printing a solid cube and measuring its volume and weight. The beam diameter for each printed structure was estimated by weighing the structure and dividing the mass by the material's density to calculate the volume. Then, the relationship between the beam diameter and the actual volume was established, and simulations were conducted on structures with the estimated beam diameters rather than the CAD ones.

2.7. Experimental force data processing

The force at each constant displacement step is expected to asymptotically approach a constant value [32]. Therefore, for each displacement step, the corresponding equilibrium force was computed as the force predicted at infinite time, based on an exponential decay model. We used MATLAB's curve fitting tool (The Mathworks Inc., Natick, MA, USA) to fit the experimental force measurements to a two-term exponential function:

$$F(t) = C_1 e^{-k_1 t} + C_2 e^{-k_2 t} + F_\infty \tag{14}$$

where $F(t)$ is the force value at time t, C_1 and C_2 are the amplitudes of the two exponential terms, k_1 and k_2 are the decay constants for each term, representing the rate at which the corresponding exponential terms decay, and F_∞ is the constant value that the force asymptotically approaches as $t \to \infty$, which is considered the equilibrium force.

2.8. Measurement of full-field displacements

To obtain accurate local displacement measurements during the tests, we utilized 3D-DIC, a non-contact optical method that provides full-field measurements. The 3D-DIC setup is shown in Figure 3c and consists of two Blackfly BFS-U3-51SM-C cameras (FLIR LLC, Wilsonville, OR, USA) featuring a 5-megapixel monochrome Sony IMX264 sensor each equipped with a FUJINON HF25SA-1 lens with a focal length of 25 mm. The cameras were configured in a stereo arrangement and synchronized to capture simultaneous images of the test specimens at each displacement step. The images were acquired and stored using QS-GRABBER software (MatchID Nv, Gent, Belgium). One camera was positioned perpendicular to the specimen's measured surface, and the second was placed at a stereo angle of 23°. The standoff distance between the cameras and the specimen was 350 mm. The specimens were manually painted with a random speckle pattern of average size 2.5 mm using black ink, as shown in Figure 3b.

The intrinsic and extrinsic parameters of the cameras were calibrated using a calibration target measuring 9×12 cm with a grid of 9x12 5 mm diameter dots, using the MatchID stereo calibration software. The images were processed using MatchID STEREO software to obtain full-field displacement maps, using the following processing parameters: a subset size of 21 pixels, a step size of 10 pixels, an affine subset shape function, and Gaussian filtering with a kernel size of 5.

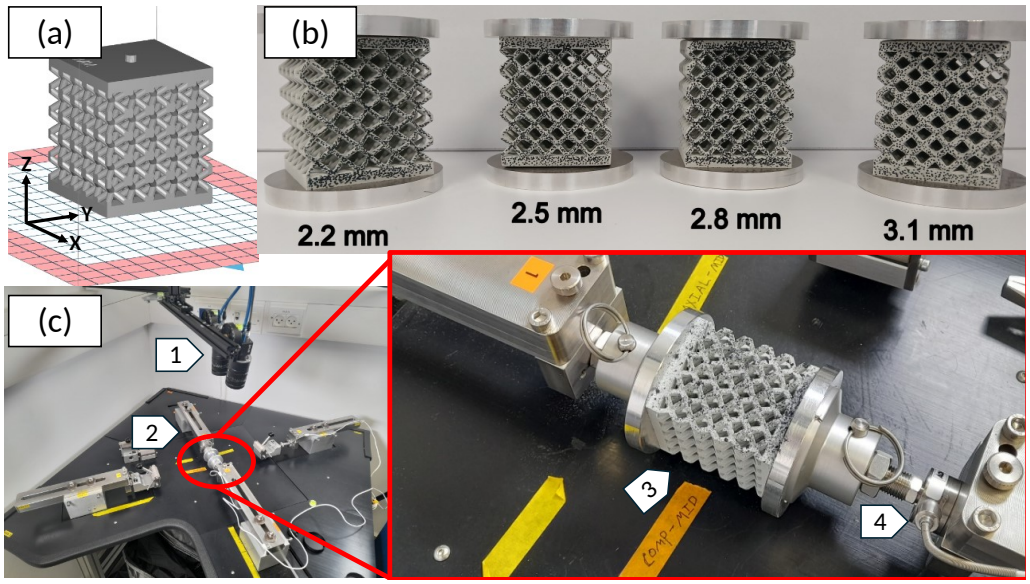

Figure 3: Lattice structures manufacturing and experimental setup: (a) Lattice structure CAD model in the printer's build volume showing the print orientation. The layers are built along the Z direction, and the printer's powder recoater moves along the Y direction. (b) SLS 3D-printed lattice structures with varying beam diameters. An aluminum adapter was adhesively bonded to each flat end of the structure to facilitate mounting in the compression test machine. (c) Experimental setup. (1) Two cameras in a stereo configuration. (2) Horizontal planar biaxial testing system. The inset on the right shows a zoomed-in view of the (3) lattice structure painted with a random speckle pattern mounted on the planar test machine grips, and (4) the 2 kN load cell.

2.9. Compression FE simulations on cubic lattice structures

Similarly to the simulations of the unit cells described in subsection 2.4, FE simulations for the lattice structures were constructed using Ansys. FE simulations of the homogenized structure were conducted using FEBio version 4.4.0 [33], with GIBBON MATLAB toolbox version 3.5.0 [34] for pre- and post-processing. The homogenized structure was meshed with 8-node trilinear hexahedral elements (hex8 in FEBio) of the corresponding unit cell size, and assigned the Fung model parameters (Fung-ortho-compressible in FEBio) obtained in the homogenization fitting process. All the simulations were performed using a Windows PC equipped with an Intel Core i7 CPU and 32 GB RAM.

The boundary conditions for the simulations are illustrated in Figure 4. SIM-1 represents the simulation of the full-geometry structure, including the solid plates used for the experiments. SIM-2 represents the simulation of the full-geometry structure used for comparison with the simulations of the homogenized model (HOM). In all the simulations, displacements were prescribed in the ±Y direction, and applied to the nodes located on the ±Y boundaries (marked in blue in Figure 4), while the same nodes were fully constrained in the X and Z directions. For SIM-1, the displacement values and the number of displacement steps were selected to match those measured during the experiments. The mesh and simulation results were imported from Ansys to MATLAB using *ANSYSimport* [35].

The key nodes (marked with red dots in Figure 4) are defined at the internal intersection points between adjacent lattice unit cells, located on the outer surface at the center of each junction where four diagonal struts converge. These nodes are used to evaluate the differences between the experimental and simulated results, as described in subsection 2.11.

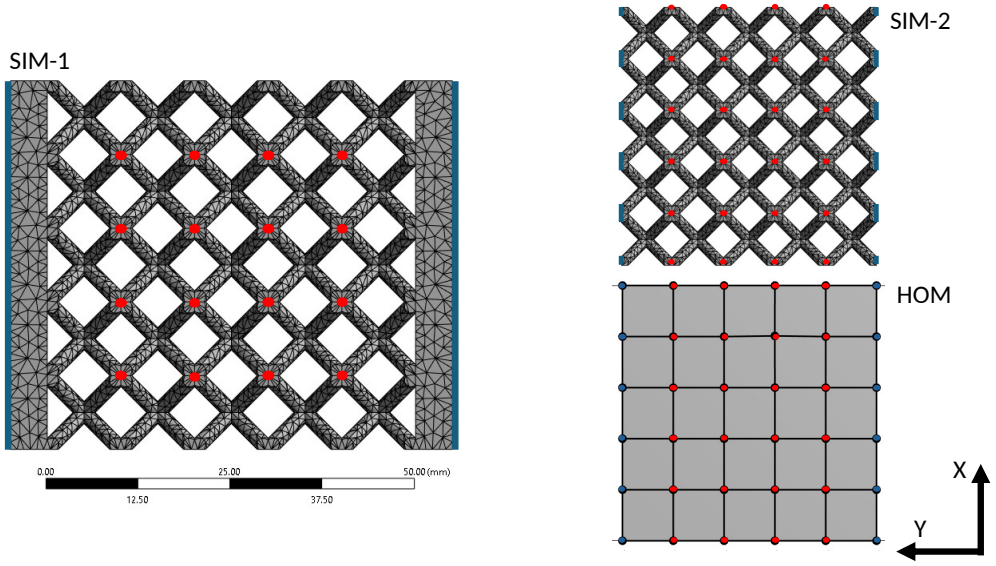

Figure 4: FE simulation boundary conditions of a lattice structure composed of cubic unit cells subjected to compressive loading. SIM-1 is the full-geometry simulation that represents the lattice structures used in the experiments (EXP), and SIM-2 is the full-geometry simulation to be compared with the homogenized simulation (HOM). Displacements in the Y direction, marked in blue, were prescribed to the nodes located on the ±Y boundaries of each model, while the same nodes were fully constrained in the X and Z directions. The key nodes for comparison between the experimental, simulation, and homogenization results are marked with red dots.

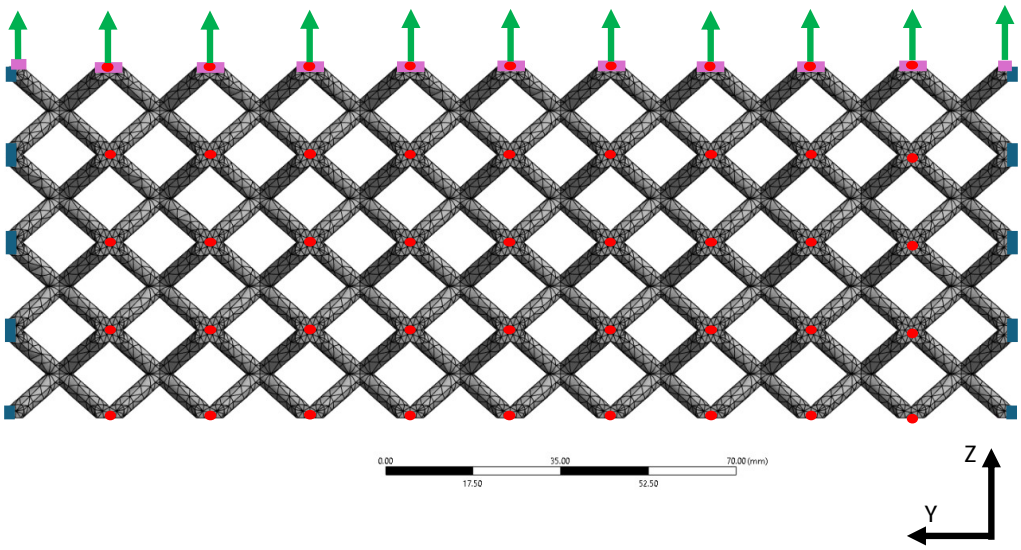

Figure 5: FE simulation model of lattice beam structure composed of orthotropic unit cells. Distributed load, illustrated by green arrows, is applied to nodes on the upper surface, marked in pink, while the nodes on the sides, marked in blue, are fixed. The key nodes for comparison with the homogenized simulation are marked with red dots.

2.10. Demonstrative FE simulation with multiple deformation modes

To evaluate the capability of our homogenization process to capture the mechanical response in a more complex case, we designed a short beam with $4 \times 10 \times 4$ orthotropic unit cells, each with dimensions of $15 \times 20 \times 17\,\text{mm}^3$ in the X, Y, and Z directions, respectively, and a uniform beam diameter $D = 3.5\ mm$. The beam was subjected to a distributed force in the Z direction, which was applied to all nodes on the upper surface, while all DOFs were fully constrained on all nodes on the side surfaces, as illustrated in Figure 5. The force was linearly increased from 0 N to 300 N in 10 equally spaced steps. Similarly to the simulations of the cubic structures, two equivalent FE simulations were constructed: the full lattice geometry simulated in Ansys, and a homogenized simulation conducted in FEBio, using the homogenized parameters found through the methods described in subsection 2.4.

2.11. Evaluation of the accuracy of the homogenization process

To evaluate the accuracy of the homogenization process, we compare both the reaction forces and the displacements at key nodes. The displacement comparison between the homogenized model (HOM) and the full-geometry simulation SIM2 includes all the key nodes. The comparison between the SIM1 and the experimental measurements (EXP) is restricted to the key nodes positioned in the central region, as illustrated in Figure 4, because some of the nodes where the lattice structure is connected to the solid plate were obscured in the DIC images by the platens of the testing machine.

To evaluate the quality of agreement between the experimental, simulation, and homogeniza-

tion reaction force results, the normalized force differences are defined by:

$$\Delta F_{\text{tot}}^{\text{EXP-SIM1}}[\%] = 100 \cdot \frac{1}{N_{\text{steps}}} \sum_{i=1}^{N_{\text{steps}}} \frac{\left|F_i^{\text{EXP}} - F_i^{\text{SIM1}}\right|}{\left|F_{N_{\text{steps}}}^{\text{EXP}}\right|} \tag{15a}$$

$$\Delta F_{\text{tot}}^{\text{SIM2-HOM}}[\%] = 100 \cdot \frac{1}{N_{\text{steps}}} \sum_{i=1}^{N_{\text{steps}}} \frac{\left|F_i^{\text{SIM2}} - F_i^{\text{HOM}}\right|}{\left|F_{N_{\text{steps}}}^{\text{SIM2}}\right|} \tag{15b}$$

where N_{steps} is the number of displacement steps, N_n is the number of key nodes in the structure, F_i is the force in the displacement step i.

Similarly, the normalized displacement differences are defined by:

$$\Delta u_{\text{tot}}^{\text{EXP-SIM1}}[\%] = 100 \cdot \frac{1}{N_{\text{steps}}} \frac{1}{N_n} \sum_{i=1}^{N_{\text{steps}}} \sum_{j=1}^{N_n} \frac{\left|\mathbf{u}_{i,j}^{\text{EXP}} - \mathbf{u}_{i,j}^{\text{SIM1}}\right|}{\left|\mathbf{u}_{N_{\text{steps}},j}^{\text{EXP}}\right|} \tag{16a}$$

$$\Delta u_{\text{tot}}^{\text{SIM2-HOM}}[\%] = 100 \cdot \frac{1}{N_{\text{steps}}} \frac{1}{N_n} \sum_{i=1}^{N_{\text{steps}}} \sum_{j=1}^{N_n} \frac{\left|\mathbf{u}_{i,j}^{\text{SIM2}} - \mathbf{u}_{i,j}^{\text{HOM}}\right|}{\left|\mathbf{u}_{N_{\text{steps}},j}^{\text{SIM2}}\right|} \tag{16b}$$

where $\mathbf{u}_{i,j}$ denotes the displacement vector of the key node j in the displacement step i.

To allow for a direct comparison between experimental and simulated results, the coordinate systems in which they are described must be identical. Therefore, a 3D rigid body transformation is applied to align the experimental data with the simulation coordinate system. This is achieved by matching the experimental and simulated point clouds of the outer surfaces that are visible in the DIC cameras, in the reference (unloaded) configuration, using the iterative closest point (ICP) algorithm [36], implemented via MATLAB's *pcregistericp* function. Then, since experimental DIC points and the simulation nodes do not perfectly align, the DIC data is interpolated at the positions of the FE nodes using their local barycentric coordinates within the triangular faces on the outer surfaces of the simulation elements [37]. Even after transformation and interpolation, initial positional differences may exist. This error is quantified using average initial positional difference Δ_0^{avg}, defined as:

$$\Delta_0^{\text{avg}} = \frac{1}{N_n} \sum_{j=1}^{N_n} \left|\mathbf{x}_{0,j}^{\text{EXP}} - \mathbf{x}_{0,j}^{\text{SIM1}}\right| \tag{17}$$

where $\mathbf{x}_{0,j}$ denotes the position vector of the key node j in the initial configuration step.

3. Results

3.1. Lattice structure beam diameters

Table 1 presents the values of the lattice structures' beam diameters, as computed using the method described in subsection 2.6. The measured density of the printed TPU material is 1.07 g/cm^3 [28], compared to the manufacturer's declared value of 0.95 g/cm^3. Notably, the dimensions of the 3D-printed specimens differ from those of their CAD models. For simplicity of reading, the different unit cells and lattice structures are referred to by their nominal beam diameters, even though the FE simulations were conducted using the actual dimensions of the printed models.

Table 1: Nominal and measured beam diameters for printed lattice structures.

Measured mass [g]	Nominal diameter [mm]	Printed diameter [mm]
40.44	2.20	1.54
46.11	2.50	1.81
52.79	2.80	2.13
61.23	3.10	2.52

3.2. Unit cells homogenization results

As a compromise between the increased accuracy and elapsed times in unit cells FE simulations, we chose to use a mesh element size of 1 *mm* for all unit cells, as illustrated in Figure 2. The number of elements and nodes is described in Table 2.

Table 2: Number of elements and nodes in FE mesh for unit cells with different symmetries and beam diameters.

Unit cell symmetry	D [mm]	No. Elements [-]	No. Nodes [-]
Cubic	2.2	2926	5479
Cubic	2.5	2786	5142
Cubic	2.8	2814	5108
Cubic	3.1	2757	5005
Orthotropic	3.5	7718	13071

FE simulation results for uniaxial stretch and shear strain applied to cubic unit cells with varying beam diameters, along with the corresponding stress predictions from the fitted Fung model, are presented in Figure 6 and summarized in Table 3. FE simulation results for uniaxial stretch and shear strain applied to the orthotropic unit cell at different directions, along with the corresponding stress predictions from the fitted Fung model, are presented in Figure 7 and summarized in Table 4.

Table 3: Summary of Fung model fitting results, including the fitted model parameters and the coefficients of determination (R^2), for cubic unit cells with various beam diameters (D).

D [mm]	R^2 [-]	E [kPa]	ν [-]	G [kPa]	κ [kPa]	c_0 [kPa]
2.2	0.9964	56	0.454	269	0	162
2.5	0.9975	113	0.450	377	0	329
2.8	0.9980	230	0.447	533	0	687
3.1	0.9982	469	0.425	754	0	1411

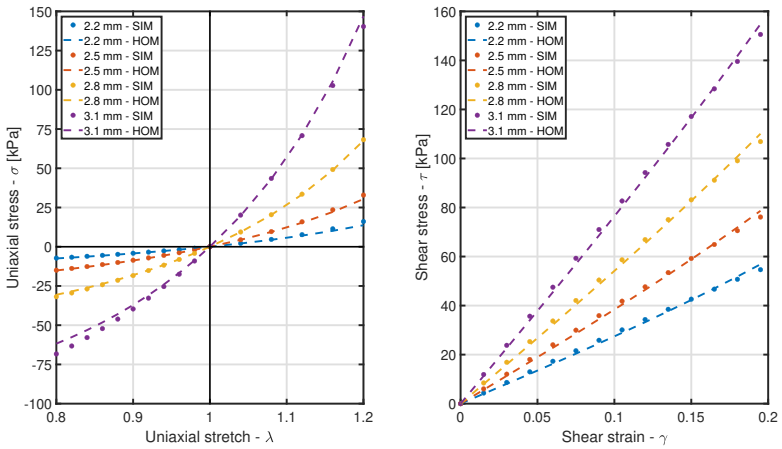

Figure 6: A comparison of stress responses from FE simulations and a homogenized model is presented for cubic unit cells with various beam diameters subjected to uniaxial tension and compression (left), as well as simple shear (right). The stresses obtained from FE simulations are represented by solid dots, and the Fung model fitted values are indicated by a dashed line.

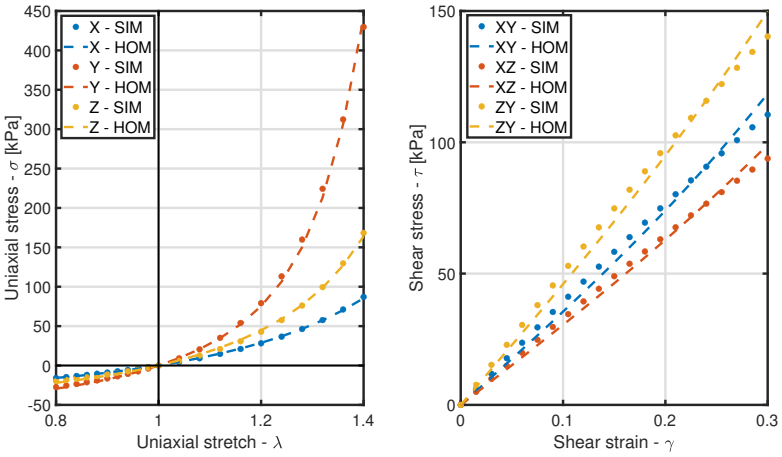

Figure 7: A comparison of the stress responses from FE simulations and a homogenized model is presented for an orthotropic unit cell subjected to uniaxial tension and compression (left), as well as simple shear (right) in the three principal directions. The stresses obtained from FE simulations are represented by solid dots, and the Fung model fitted values are indicated by a dashed line.

Table 4: Summary of Fung model fitting results for the orthotropic unit cell, including the fitted model parameters and the coefficients of determination (R^2) .

R^2 [-]	E_{11} [kPa]	E_{22} [kPa]	E_{33} [kPa]	G_{12} [kPa]	G_{23} [kPa]	G_{31} [kPa]	ν_{12} [-]	ν_{23} [-]	ν_{31} [-]	κ [kPa]	c_0 [kPa]
0.9990	105.0	237.3	152.1	350.1	454.8	301.7	0.273	0.675	0.483	0.0	1.78×10^8

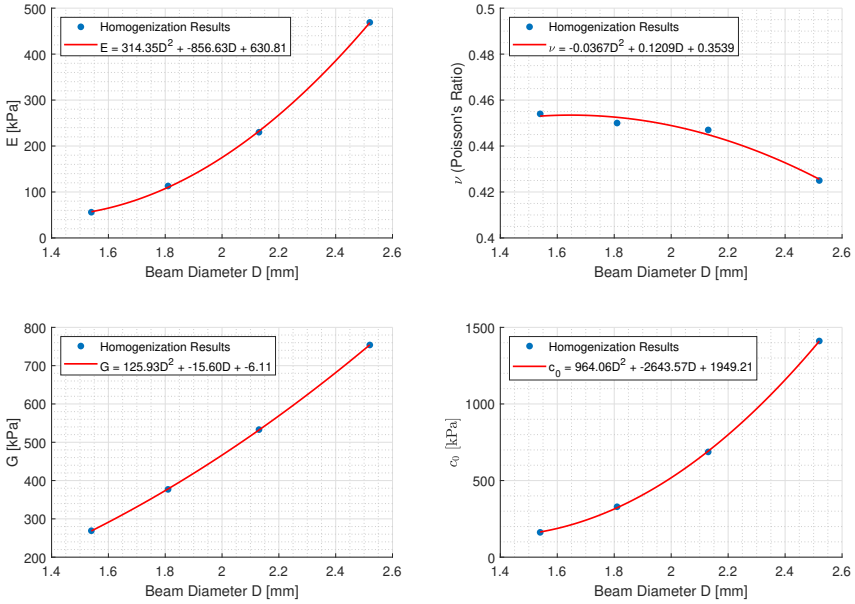

Figure 8: Fung model parameters E, G, ν, c_0 as a function of beam diameter (D) for a BC unit cell. The fitting equation for each curve is also shown within the figure.

The dependency of the cubic Fung constitutive model parameters (E, G, ν, and c_0) on the beam diameter (D), based on the results listed in Table 3, was analyzed and fitted using second-order polynomial functions, as shown in Figure 8. These fitting results can be used to estimate the Fung cubic constitutive model parameters for other values of beam diameters.

Although this research focuses on BC lattice structures, a wide variety of other topologies exist (see, for example, [38]). To evaluate the generalizability of our methodology, we examined the fitting of the Fung constitutive model to two additional lattice topologies: cube and octagonal unit cells. Each unit cell had a size of $10\times10\times10\,\text{mm}^3$, with beam diameters of 3 *mm* for the cube and 1.5 *mm* for the octagonal unit cell. We employed the same PBC outlined in subsection 2.2 and constitutive model described in subsection 2.3. Figure 9 presents the resulting uniaxial and shear stress-strain relations, along with the corresponding stress predictions derived from the fitted Fung model.

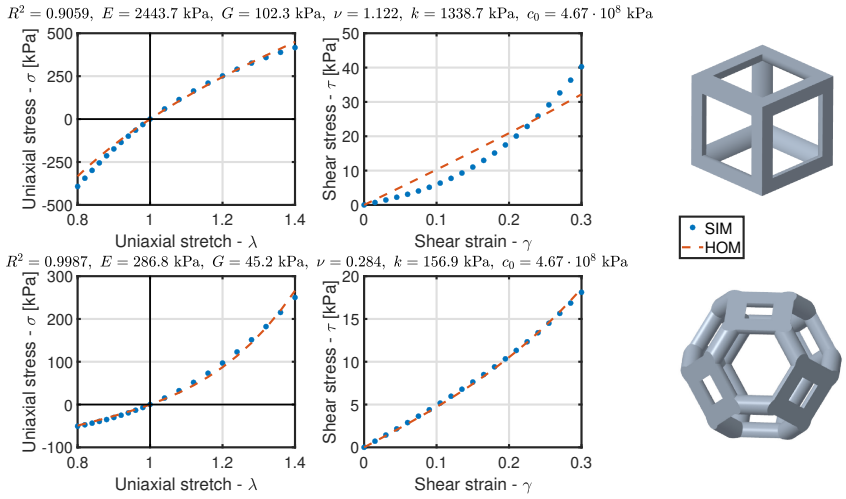

Figure 9: Homogenization analysis for cube (upper) and octagonal (lower) unit cells. The figure shows the comparison between simulation and homogenization results in uniaxial and shear deformations. The fitted Fung model parameters and the coefficient of determination (R^2) are shown for each topology.

3.3. Equilibrium force from exponential decay fitting

The relaxation behavior of the lattice structure under constant displacement was analyzed using the exponential decay model described in subsection 2.7. The equilibrium force (F_∞) for each displacement step was determined by fitting the measured force relaxation data to (14). Figure 10 illustrates exemplary fitting results for a representative displacement step of the $D = 2.5$ *mm* lattice structure. The measured force data points are plotted alongside the fitted curves, demonstrating excellent agreement. Similar results were observed for all other displacement steps across all lattice structures.

3.4. Cubic lattice structures: experimental and simulation results

We compared the results obtained from the experiments, simulation of the full lattice geometry, and simulation of the homogenized model. The simulation times of the full-geometry lattice structures were approximately 45 minutes, while the homogenized simulations took only a few seconds. The comparison included the reaction forces and the displacements of key nodes, as described in subsection 2.11 The compressive reaction forces are shown in Figure 11 and Figure 12, comparing experimental results with the corresponding simulations, and homogenized model predictions with simulations, respectively, across various beam diameters. During the experiments, we observed that the displacements measured using DIC at the boundaries of the structures differed slightly from those specified to the testing machine. Therefore, the displacement values prescribed in the SIM-1 simulation were adjusted to match the experimental ones, as can be seen in Figure 11.

A representative full-field displacement map, comparing the experimental results obtained using DIC with the corresponding full-geometry simulation (SIM-1), is shown in Figure 13. Similarly, Figure 14 illustrates a comparison between the full-geometry (SIM-2) and homogenized simulations. Furthermore, Figure 15 and Figure 16 depict the relative differences in the

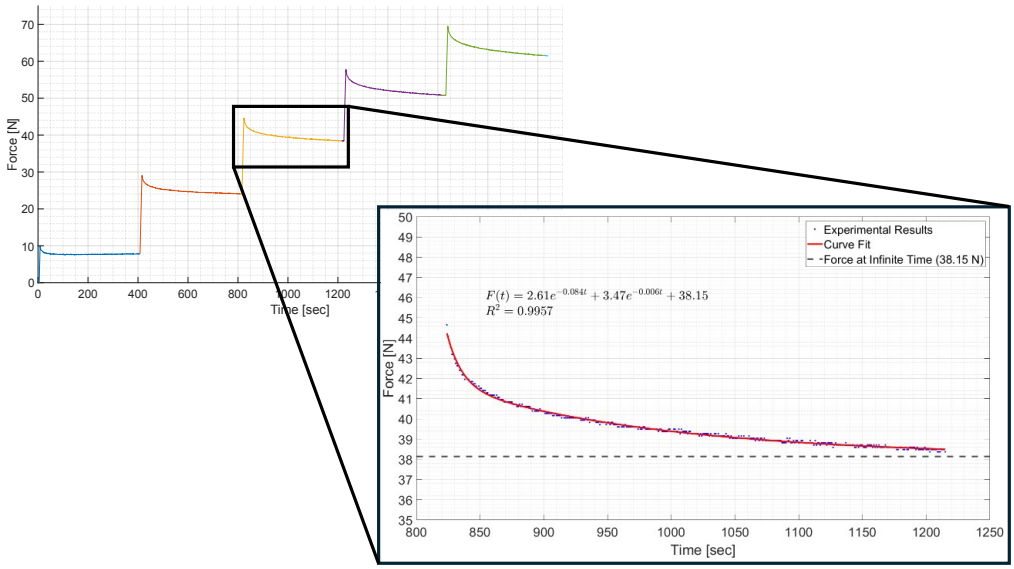

Figure 10: Force measurements of the $D = 2.5$ *mm* lattice structure during compression test, demonstrating stress relaxation. The inset shows a zoomed-in view of the relaxation behavior observed during the third displacement step, alongside its fitted exponential decay function described in (14).

displacements of the key nodes at each step of structure compression, comparing EXP versus SIM-1 results, and SIM-2 versus HOM results, respectively.

The average initial positional difference Δ_0^{avg}, as well as the relative differences in the displacements (Δu_{tot}) and force (ΔF_{tot}) are summarized in Table 5.

3.5. Simulation of beam with orthotropic unit cells

As a demonstrative case with multiple deformation modes, we compared the homogenization accuracy for a beam with orthotropic unit cells subjected to a distributed load that caused bending. As detailed in subsection 2.10, the displacements were evaluated at key nodes, as shown in Figure 5. The displacement magnitudes across the structure for the full-geometry and the homogenized simulations are shown in Figure 17 for the last simulation step. Moreover, the relative differences in the displacements of the key nodes at each force step are shown in Figure 18. The total displacement relative difference between the full-geometry and homogenized simulations is $\Delta u_{\text{tot}}^{\text{SIM-HOM}} = 7.4\%$.

4. Discussion

This study presents a numerical homogenization framework for BC lattice structures, which captures their orthotropic nonlinear elastic response under tension, compression, and shear loadings. Replacing the lattice structures with homogenized solid elements of equivalent properties substantially reduces computation time, with only a slight compromise in simulation accuracy. This enables practical analysis of large structures with numerous unit cells, facilitating rapid iterative design optimization workflows.

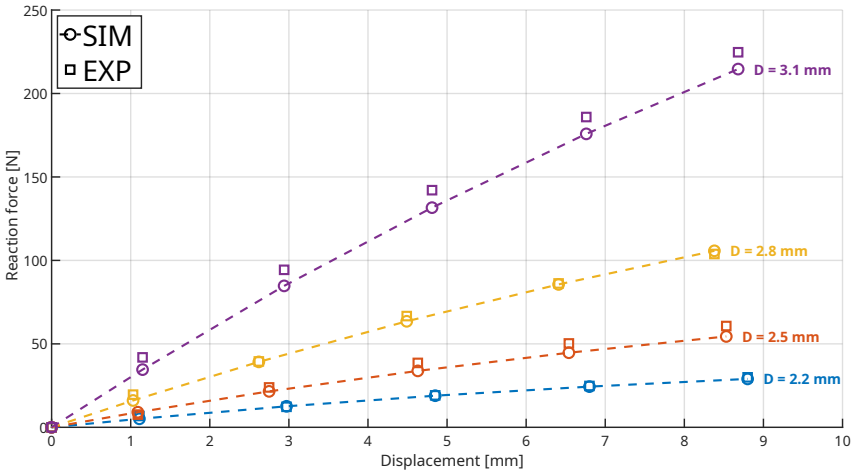

Figure 11: Comparison of compressive force-displacement results between FE simulations (SIM-1) and experiments (EXP), for four lattice structures with varying beam diameters (D).

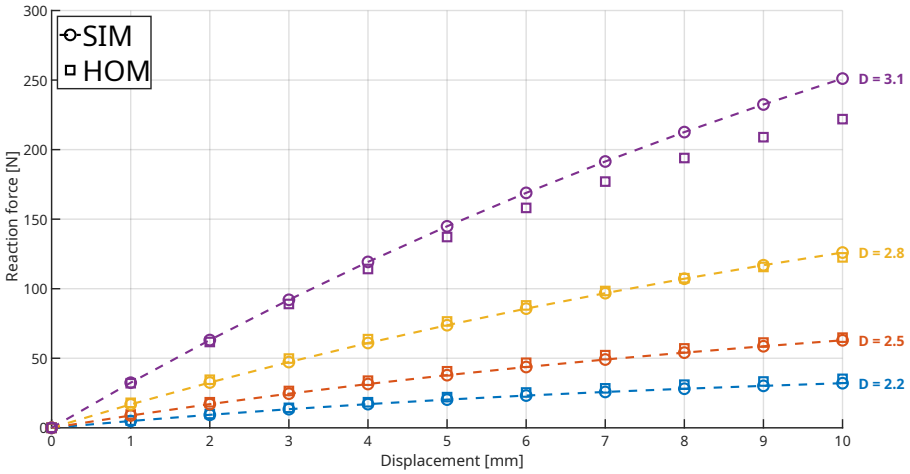

Figure 12: Comparison of compressive force-displacement results between FE simulations with full-geometry (SIM-2) and corresponding homogenized models (HOM), for four lattice structures with varying beam diameters (D).

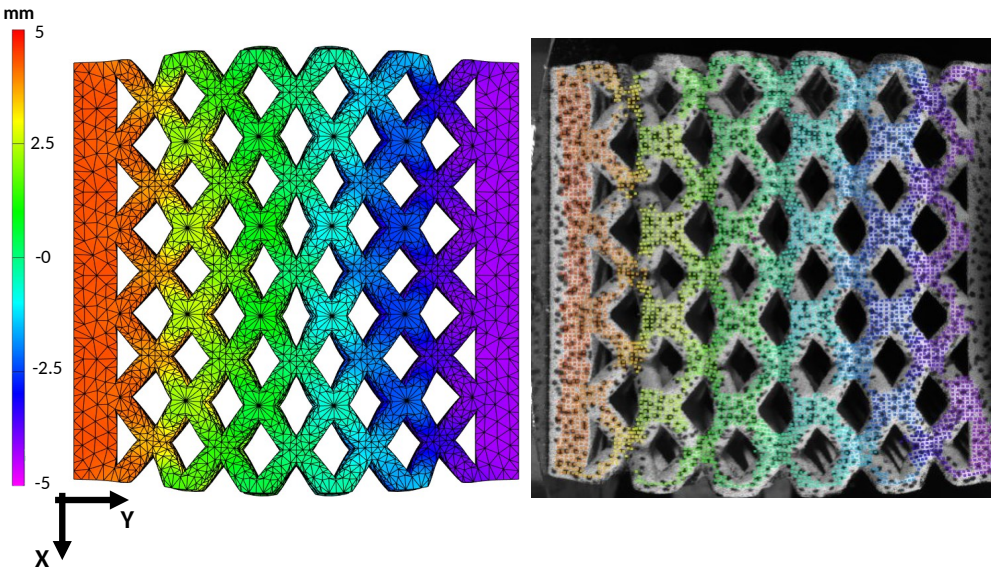

Figure 13: Full-field displacement in the Y direction for the $D = 3.1$ mm lattice structure at maximum compression, comparing the FE simulation results (left), and experimental results obtained using DIC (right).

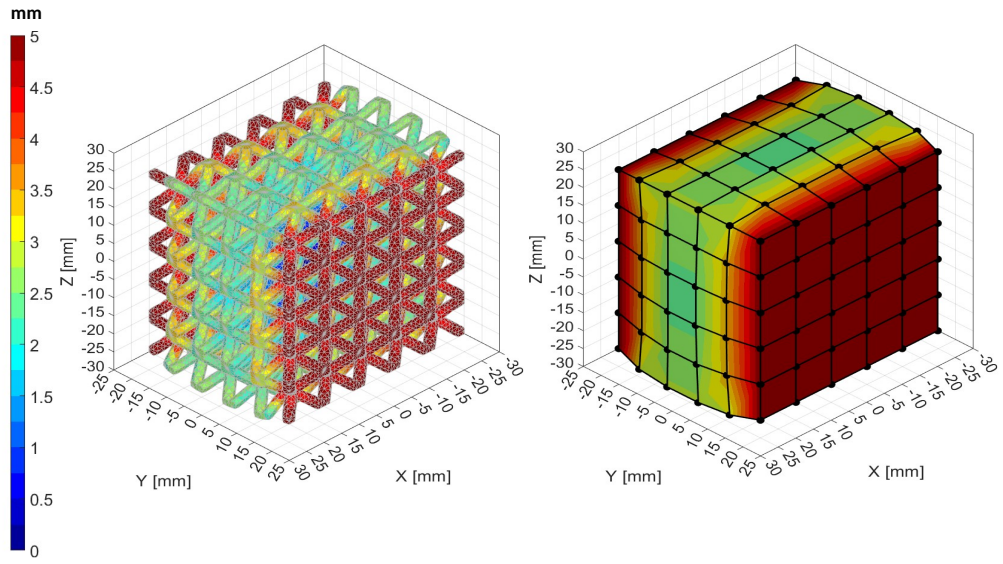

Figure 14: Displacement magnitude maps for the $D = 3.1$ *mm* lattice structure at maximum compression, comparing the FE simulation results obtained for the full-geometry model (left), and the homogenized model (right).

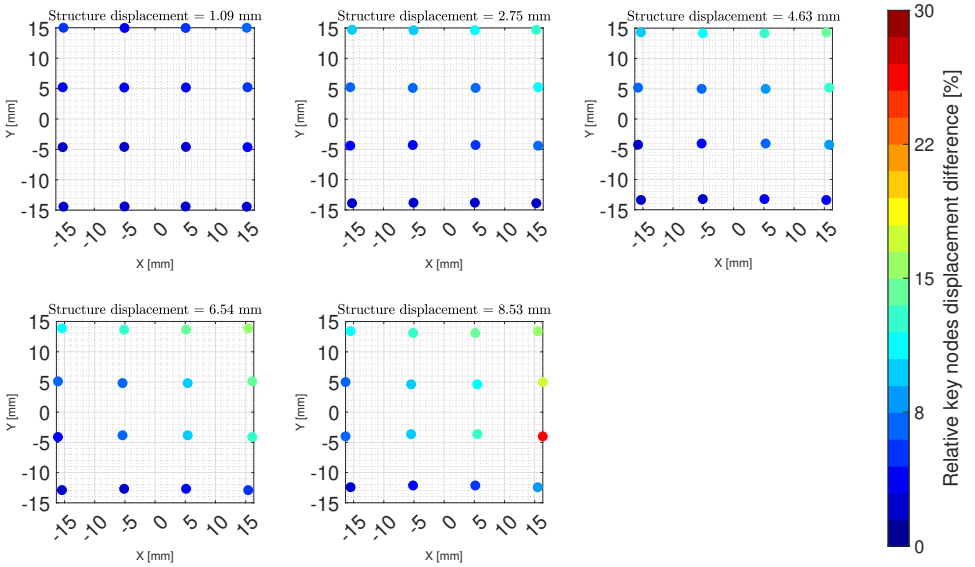

Figure 15: Relative difference in displacements between experimental and FE full-geometry simulations, at the key nodes (see Figure 4) of the $D = 2.5$ *mm* lattice structure, at each structure compression step.

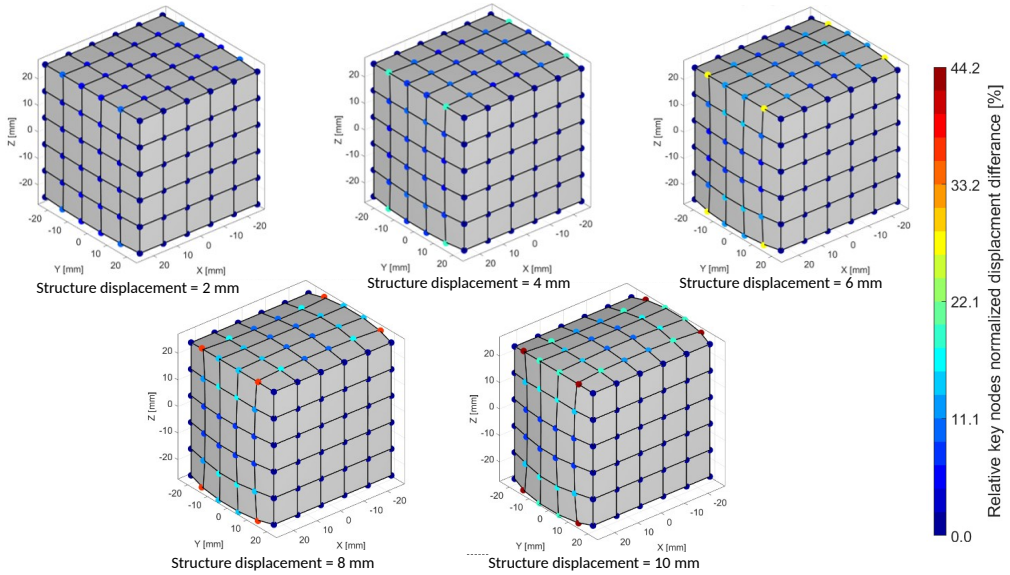

Figure 16: Relative difference in displacements between FE full-geometry simulation and homogenized simulation, at the key nodes, for the $D = 2.2$ *mm* lattice structure at multiple structure displacement steps. It can be seen that the key nodes at the edges of the structure exhibit larger displacement differences than the nodes in the center of the structure.

Table 5: Comparison of displacement and force differences between experimental (EXP), full-geometry simulation (SIM1 and SIM2), and homogenized simulation (HM) results, for various lattice structure beam diameters (D).

Nominal beam diameter D [mm]	Initial average position error $\Delta_0^{\text{avg}}[mm]$ Eq. (17)	Displacement difference $\Delta u_{\text{tot}}^{\text{EXP-SIM1}}[\%]$ Eq. (16a)	Force difference $\Delta F_{\text{tot}}^{\text{EXP-SIM1}}[\%]$ Eq. (15a)	Displacement difference $\Delta u_{\text{tot}}^{\text{SIM2-HOM}}[\%]$ Eq. (16b)	Force difference $\Delta F_{\text{tot}}^{\text{SIM2-HOM}}[\%]$ Eq. (15b)
2.2	0.3	8.1	2.3	10.7	5.9
2.5	0.3	7.3	6.4	4.7	3.6
2.8	0.2	7.1	2.4	5.8	1.6
3.1	0.3	6.3	4.2	4.1	4.5

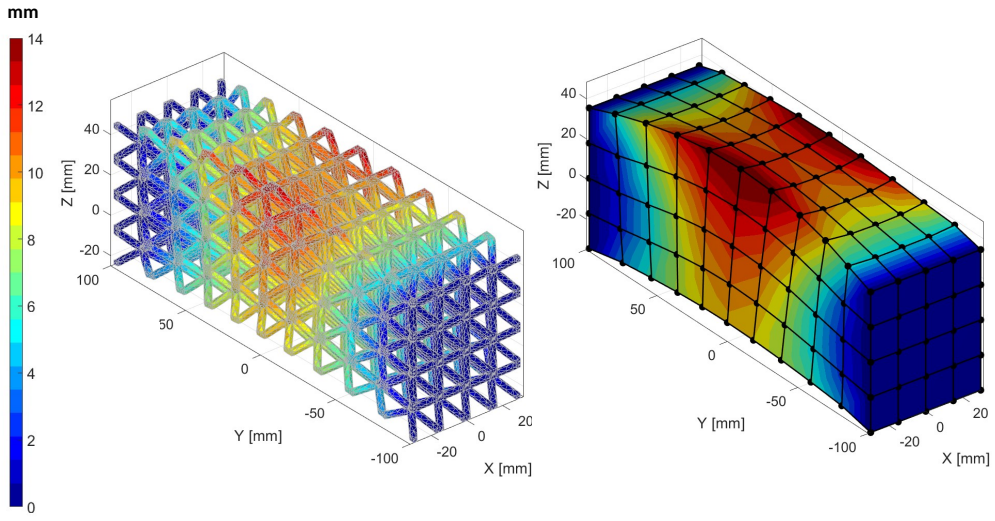

Figure 17: Displacement magnitude results for the full-geometry simulation (left) and homogenized simulation (right) of the beam with orthotropic unit cells. Results are shown for the last force step (300 N).

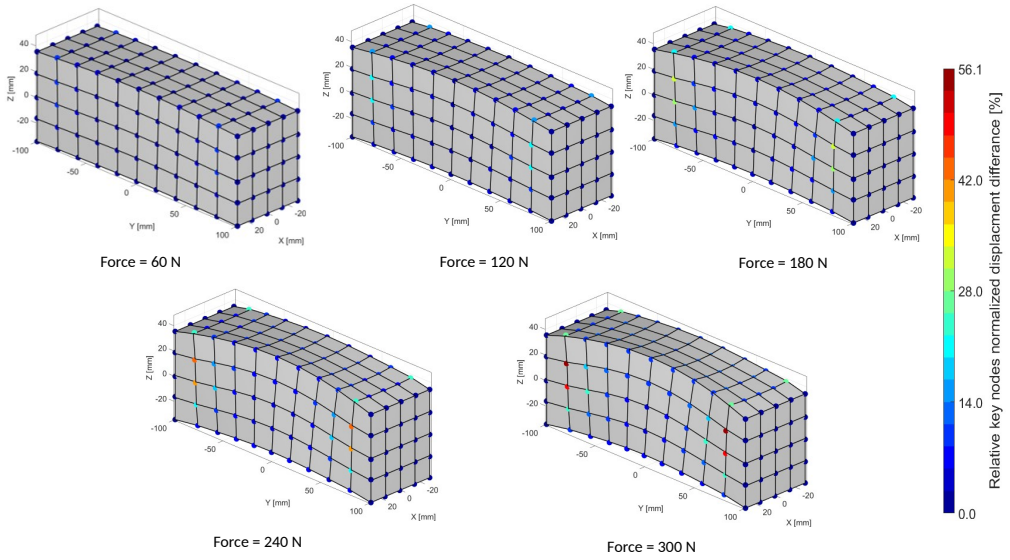

Figure 18: Relative displacement differences obtained from comparing full-geometry and homogenized simulations of the beam with orthotropic unit cells, shown for each force step.

Since this study involved experimental validation, all the FE simulations used the material parameters of the TPU powder, Flexa Bright™ 3D printed through SLS. In this study, we modeled the material as isotropic linear elastic, neglecting stiffness variations due to printing orientation and between tension and compression, as well as viscoelastic effects, which were previously found in our study [28]. This deliberate compromise was made to prioritize the simplicity of the simulations and keep the focus on the homogenization procedure. Nevertheless, future work could implement more complex models to describe the bulk material (e.g., using constitutive models that take into account orientation-dependence [39], tension-compression asymmetry [40], or viscoelasticity [41]) and evaluate their influence on the accuracy of simulations.

We fabricated BC cubic lattice structures with varying beam diameters. The measured dimensions of the beam diameters differed substantially from the nominal dimensions specified in the CAD models. This discrepancy is likely due to the specific conditions and parameters of the 3D printing process. As previously reported for other SLS printers, factors such as temperature gradients in the build chamber and differential shrinkage between adjacent layers can contribute to dimensional deviations [42, 43, 44]. Although it is possible to reduce these artifacts by optimizing the printing parameters and implementing advances in SLS technology [45], our study did not focus on minimizing the differences between the CAD models and the printed samples. Instead, we measured the dimensions of the fabricated samples, assuming a homogeneous beam diameter within each structure, and ensured this homogeneity by orienting the structures 45° relative to the build platform, as shown in Figure 3a.

Next, we conducted compression experiments during which the reaction forces and full-field displacements were measured. The experimental results were compared with the full-geometry FE simulations in which the boundary conditions replicated the experimentally measured ones. Although equal displacements were applied to both compression platens, the DIC results revealed

unexpected asymmetry. This difference was attributed to incomplete bonding between the printed plates and aluminum adapters, resulting in a gradual gap closure during loading. As a result, the actual displacements of the structure's solid plates deviated from those applied by the machine. To allow a proper comparison between experimental and simulation results, we prescribed the same displacement data measured via DIC to the solid plates in the corresponding simulations (SIM-1).

As part of the homogenization process, we conducted FE simulations of the lattice unit cells subjected to uniaxial tension-compression and simple shear, and the simulation data were fitted with a Fung hyperelastic compressible orthotropic constitutive model. The fitted parameters were used to construct FE simulations of homogenized solid structures. The results of these simulations were compared to those of the full-geometry simulations, considering both the reaction forces and displacements at key nodes, to evaluate the capability of the homogenization method to accurately capture the response of cubic lattice structures under compression and a beam with orthotropic unit cells subjected to bending.

The cubic and orthotropic BC unit cells exhibited notable nonlinear responses when subjected to uniaxial tension and compression, while the responses to simple shear were nearly linear. Capturing the homogenized response required a hyperelastic orthotropic constitutive model to accurately represent the stress-strain relationships of all deformation modes. The results presented in subsection 3.2 confirm that the Fung hyperelastic compressible orthotropic model is well suited for this task, with R^2 values greater than 0.99 for all fittings. The Fung model exhibited good fitting also to the cube and octagonal unit cells, except the cube unit cell's highly nonlinear response to simple shear was not captured as well by this model, reducing its overall R^2 value to 0.9 (see Figure 9).

The relations between the unit cells' beam diameters and the Fung model parameters (E, G, ν, and c_0) exhibited nonlinear relations, as shown in Figure 8. Fitting of polynomial functions to these relations can facilitate the estimation of constitutive parameters for other beam diameters.

To the best of our knowledge, this is the first study presenting the numerical homogenization of hyperelastic orthotropic constitutive models for thick-beam lattice structures subjected to finite multiaxial deformations. Homogenization for truss lattice structures with slender beams has been widely studied, with notable contributions by Phlipot and Kochman (2019) [12] and Fernández et al. (2021) [24]. These studies employed beam elements, which are not applicable for modeling unit cells with thick beams, such as those used in this study. Jamshidian et al. (2020) [25] homogenized the response of soft lattice structures subjected to uniaxial tension and compression, including buckling, to a Hyperfoam *isotropic* constitutive model. Both the Hyperfoam and the Fung models effectively capture the macro-scale compressibility of the structures. However, the Fung orthotropic model supplements the anisotropic behavior. Other studies that homogenized the anisotropic response of lattice structures limited their analysis to the linear elastic regime (e.g., [26, 17, 18]).

The comparison of reaction forces and displacements at key nodes across experiments, full-geometry simulations, and homogenized simulations revealed good agreements, as summarized in Table 5. Notably, the homogenized simulations require only a fraction of the computational time while maintaining accurate responses, with relative errors ranging from 4.1% to 10.7%. The agreement between the experimental results and those from full-geometry simulations indicates that modeling the SLS-printed TPU with a linear elastic material model is reasonable under quasi-static conditions, even though it does not account for the observed anisotropy and tension-compression asymmetry in the bulk material properties [28]. When comparing homogenization to full-geometry simulation, the largest discrepancies occur at the outer boundaries of the lat-

tice structure. This can be attributed to the reduced representativeness of the unit cell in these regions. The small differences observed in the reaction forces suggest that the homogenization method effectively captures the stiffness of the structures. The results presented in subsection 3.5 confirm that the homogenization method also achieves good accuracy for lattice structures with orthotropic unit cells subjected to combined deformation modes such as bending caused by a distributed load across a beam.

Various future research directions can stem from the current study. First, while we focused on BC unit cells and demonstrated that the Fung model may also be suitable for homogenizing a cube and octagonal unit cells, further investigation into other topologies and types of lattice structures (e.g., as in [26, 46, 38, 47, 25]) could expand the method's applicability. Furthermore, this study used the Fung model for homogenization, which yielded satisfactory results for the investigated unit cells. However, it is possible that other topologies may exhibit responses that cannot be fitted well with the Fung model. Therefore, future work could incorporate machine learning-based discovery of suitable material models, as previously suggested by various researchers (e.g., [48, 49, 50]). Furthermore, in this study, we used the equilibrium force and excluded data collected during stress relaxation when fitting the hyperelastic effective response. Future research could integrate viscoelastic models to account for the observed time-dependent responses. Future work could also integrate the proposed homogenization method into iterative design frameworks, which are currently mostly limited to linear elasticity [51, 11]. This integration could enable the optimization of lattice structures based on user-defined performance criteria, particularly in applications that necessitate soft structures, such as those that interface with soft tissues (e.g., [3, 5, 7, 9]).

Acknowledgements

This work was supported by grant 1021190 from PTC and the Technion Additive Manufacturing Center (TAMC). The funders had no role in study design, data collection and analysis, decision to publish, or preparation of the manuscript.

References

[1] K. V. Wong, A. Hernandez, A Review of Additive Manufacturing, ISRN Mechanical Engineering 2012 (2012) 1–10. doi:10.5402/2012/208760.

[2] G. Dong, Y. Tang, Y. F. Zhao, A survey of modeling of lattice structures fabricated by additive manufacturing, Journal of Mechanical Design, Transactions of the ASME 139 (2017) 1–13. doi:10.1115/1.4037305.

[3] G. Dong, D. Tessier, Y. F. Zhao, Design of shoe soles using lattice structures fabricated by additive manufacturing, Proceedings of the International Conference on Engineering Design, ICED 2019-Augus (2019) 719–728. doi:10.1017/dsi.2019.76.

[4] O. Ulerich, S. Cananau, D. A. Prisecaru, M. Mărgăritescu, C.-S. Negrea, Design of Customized Shoe Soles Using Lattice Structures Fabricated by Additive Manufacturing, in: A. Burduk, A. D. L. Batako, J. Machado, R. Wyczółkowski, E. Dostatni, I. Rojek (Eds.), Intelligent Systems in Production Engineering and Maintenance III, Springer Nature Switzerland, Cham, 2024, pp. 209–228. doi:10.1007/978-3-031-44282-7_17.

[5] Y. Sterman, D. Solav, N. Rosen, E. Saffuri, L. Shmilov Zaritsky, Custom orthotic insoles with gradual variable stiffness using 3D printed spacer technique, Virtual and Physical Prototyping 19 (2024) e2336151. URL: https://doi.org/10.1080/17452759.2024.2336151. doi:10.1080/17452759.2024.2336151, publisher: Taylor & Francis _eprint: https://doi.org/10.1080/17452759.2024.2336151.

[6] Z. Ma, J. Lin, X. Xu, Z. Ma, L. Tang, C. Sun, D. Li, C. Liu, Y. Zhong, L. Wang, Design and 3D printing of adjustable modulus porous structures for customized diabetic foot insoles, International Journal of Lightweight Materials and Manufacture 2 (2019) 57–63. URL: https://www.sciencedirect.com/science/article/pii/S2588840418300477. doi:10.1016/j.ijlmm.2018.10.003.

[7] H. M. Herr, K. M. Moerman, D. Solav, B. J. Ranger, R. Steinmeyer, S. L. Ku, C. Dagdeviren, M. Carney, G. A. Prieto-Gomez, X. Zhang, others, Quantitative Design and Manufacturing Framework for a Biomechanical Interface Contacting a Biological Body Segment, 2021.

[8] P. Rai, V. Jankiraman, M. Teacher, R. Velu, S. Anand Kumar, T. Binedell, K. Subburaj, Design and optimization of a 3D printed prosthetic socket for transtibial amputees, Materials Today: Proceedings 70 (2022) 454–464. URL: https://www.sciencedirect.com/science/article/pii/S2214785322061818. doi:10.1016/j.matpr.2022.09.365.

[9] S. De La Rosa, P. F. Mayuet, J. Ramón, M. Salgueiro, L. Rodríguez-Parada, Design of Customized TPU Lattice Structures for Additive Manufacturing: Influence on the Functional Properties in Elastic Products (2021). URL: https://doi.org/10.3390/polym13244341. doi:10.3390/polym13244341.

[10] A. Vigliotti, V. S. Deshpande, D. Pasini, Non linear constitutive models for lattice materials, Journal of the Mechanics and Physics of Solids 64 (2014) 44–60. URL: https://linkinghub.elsevier.com/retrieve/pii/S0022509613002238. doi:10.1016/j.jmps.2013.10.015.

[11] G. Savio, A. Curtarello, S. Rosso, R. Meneghello, G. Concheri, Homogenization driven design of lightweight structures for additive manufacturing, International Journal on Interactive Design and Manufacturing (IJIDeM) 13 (2019) 263–276. URL: http://link.springer.com/10.1007/s12008-019-00543-0. doi:10.1007/s12008-019-00543-0.

[12] G. P. Phlipot, D. M. Kochmann, A quasicontinuum theory for the nonlinear mechanical response of general periodic truss lattices, Journal of the Mechanics and Physics of Solids 124 (2019) 758–780. Publisher: Elsevier.

[13] S.-I. Park, D. W. Rosen, S.-k. Choi, C. E. Duty, Effective mechanical properties of lattice material fabricated by material extrusion additive manufacturing, Additive Manufacturing 1 (2014) 12–23. Publisher: Elsevier.

[14] D. W. Rosen, Computer-aided design for additive manufacturing of cellular structures, Computer-Aided Design and Applications 4 (2007) 585–594. Publisher: Taylor & Francis.

[15] R. Gümrük, R. Mines, Compressive behaviour of stainless steel micro-lattice structures, International Journal of Mechanical Sciences 68 (2013) 125–139. Publisher: Elsevier.

[16] J. Wallach, L. Gibson, Mechanical behavior of a three-dimensional truss material, International Journal of Solids and Structures 38 (2001) 7181–7196. Publisher: Elsevier.

[17] O. Weeger, Numerical homogenization of second gradient, linear elastic constitutive models for cubic 3D beam-lattice metamaterials, International Journal of Solids and Structures 224 (2021) 111037. URL: https://www.sciencedirect.com/science/article/pii/S0020768321001153. doi:10.1016/j.ijsolstr.2021.03.024.

[18] T. Gärtner, M. Fernández, O. Weeger, Nonlinear multiscale simulation of elastic beam lattices with anisotropic homogenized constitutive models based on artificial neural networks, Computational Mechanics 68 (2021) 1111–1130. URL: https://doi.org/10.1007/s00466-021-02061-x. doi:10.1007/s00466-021-02061-x.

[19] Y. Chen, T. Li, Z. Jia, F. Scarpa, C.-W. Yao, L. Wang, 3D printed hierarchical honeycombs with shape integrity under large compressive deformations, Materials & Design 137 (2018) 226–234. Publisher: Elsevier.

[20] Y. Jiang, Q. Wang, Highly-stretchable 3D-architected mechanical metamaterials, Scientific reports 6 (2016) 34147. Publisher: Nature Publishing Group UK London.

[21] L. Beex, R. Peerlings, M. Geers, A quasicontinuum methodology for multiscale analyses of discrete microstructural models, International Journal for Numerical Methods in Engineering 87 (2011) 701–718. Publisher: Wiley Online Library.

[22] H. Liu, J. Lv, An equivalent continuum multiscale formulation for 2D geometrical nonlinear analysis of lattice truss structure, Composite Structures 160 (2017) 335–348. Publisher: Elsevier.

[23] A. Damanpack, M. Bodaghi, W. Liao, Experimentally validated multi-scale modeling of 3D printed hyper-elastic lattices, International Journal of Non-Linear Mechanics 108 (2019) 87–110. URL: https://linkinghub.elsevier.com/retrieve/pii/S0020746218300842. doi:10.1016/j.ijnonlinmec.2018.10.008.

[24] M. Fernández, M. Jamshidian, T. Böhlke, K. Kersting, O. Weeger, Anisotropic hyperelastic constitutive models for finite deformations combining material theory and data-driven approaches with application to cubic lattice metamaterials, Computational Mechanics 67 (2021) 653–677. URL: http://link.springer.com/10.1007/s00466-020-01954-7. doi:10.1007/s00466-020-01954-7.

[25] M. Jamshidian, N. Boddeti, D. Rosen, O. Weeger, Multiscale modelling of soft lattice metamaterials: Micromechanical nonlinear buckling analysis, experimental verification, and macroscale constitutive behaviour, International Journal of Mechanical Sciences 188 (2020) 105956. URL: https://linkinghub.elsevier.com/retrieve/pii/S002074032032419X. doi:10.1016/j.ijmecsci.2020.105956.

[26] S. Xu, J. Shen, S. Zhou, X. Huang, Y. M. Xie, Design of lattice structures with controlled anisotropy, Materials and Design 93 (2016) 443–447. doi:10.1016/j.matdes.2016.01.007, publisher: Elsevier.

[27] M. Shojaee, I. Valizadeh, D. K. Klein, P. Sharifi, O. Weeger, Multiscale modeling of functionally graded shell lattice metamaterials for additive manufacturing, Engineering with Computers 40 (2024) 2019–2036. URL: https://link.springer.com/10.1007/s00366-023-01906-8. doi:10.1007/s00366-023-01906-8.

[28] D. Raf, I. Magen, L. Jordan, D. Solav, Characterization of the mechanical properties of TPU fabricated by SLS in different printing orientations, engrxiv (2025). doi:https://doi.org/10.31224/4689.
[29] Y. C. Fung, K. Fronek, P. Patitucci, Pseudoelasticity of arteries and the choice of its mathematical expression, American Journal of Physiology-Heart and Circulatory Physiology 237 (1979) H620–H631. URL: https://journals.physiology.org/doi/abs/10.1152/ajpheart.1979.237.5.h620. doi:10.1152/ajpheart.1979.237.5.H620, publisher: American Physiological Society.
[30] J. D. Humphrey, Cardiovascular solid mechanics: cells, tissues, and organs, Springer Science & Business Media, 2013.
[31] L. Mullins, Softening of rubber by deformation, Rubber chemistry and technology 42 (1969) 339–362. doi:10.5254/1.3539210.
[32] W. Fliigge, Viscoelasticity, Blaisdell Publ. Comp., London (1967) 1069–1084. Publisher: Springer.
[33] S. Maas, B. Ellis, G. Ateshian, J. Weiss, FEBio: Finite elements for biomechanics, Journal of Biomechanical Engineering 134 (2012) 011005. doi:10.1115/1.4005694.
[34] K. M. Moerman, GIBBON: the geometry and image-based bioengineering add-on, Journal of Open Source Software 3 (2018) 506.
[35] Mikkel Pedersen, ANSYSimport, 2025. URL: https://www.mathworks.com/matlabcentral/fileexchange/66659-ansysimport.
[36] P. J. Besl, N. D. McKay, Method for registration of 3-D shapes, in: Sensor fusion IV: control paradigms and data structures, volume 1611, Spie, 1992, pp. 586–606.
[37] M. S. Floater, Generalized barycentric coordinates and applications, Acta Numerica 24 (2015) 161–214. Publisher: Cambridge University Press.
[38] A. Parisien, M. S. ElSayed, H. Frei, Mechanoregulation modelling of stretching versus bending dominated periodic cellular solids, Materials Today Communications 33 (2022) 104315. URL: https://linkinghub.elsevier.com/retrieve/pii/S2352492822011576. doi:10.1016/j.mtcomm.2022.104315.
[39] X. Guo, E. Wang, H. Yang, W. Zhai, Mechanical characterization and constitutive modeling of additively-manufactured polymeric materials and lattice structures, Journal of the Mechanics and Physics of Solids 189 (2024) 105711. URL: https://www.sciencedirect.com/science/article/pii/S0022509624001777. doi:10.1016/j.jmps.2024.105711.
[40] K. M. Moerman, C. K. Simms, T. Nagel, Control of tension–compression asymmetry in Ogden hyperelasticity with application to soft tissue modelling, Journal of the Mechanical Behavior of Biomedical Materials 56 (2016) 218–228. URL: https://linkinghub.elsevier.com/retrieve/pii/S1751616115004452. doi:10.1016/j.jmbbm.2015.11.027.
[41] H. Liu, G. A. Holzapfel, B. H. Skallerud, V. Prot, Anisotropic finite strain viscoelasticity: Constitutive modeling and finite element implementation, Journal of the Mechanics and Physics of Solids 124 (2019) 172–188. URL: https://www.sciencedirect.com/science/article/pii/S0022509618303223. doi:10.1016/j.jmps.2018.09.014.
[42] M. Fahad, N. Hopkinson, Evaluation and comparison of geometrical accuracy of parts produced by sintering-based additive manufacturing processes, The International Journal of Advanced Manufacturing Technology 88 (2017) 3389–3394. Publisher: Springer.
[43] H.-J. Yang, P.-J. Hwang, S.-H. Lee, A study on shrinkage compensation of the SLS process by using the Taguchi method, International Journal of Machine Tools and Manufacture 42 (2002) 1203–1212. URL: https://linkinghub.elsevier.com/retrieve/pii/S0890695502000706. doi:10.1016/S0890-6955(02)00070-6.
[44] P. Mantada, R. Mendricky, J. Safka, PARAMETERS INFLUENCING THE PRECISION OF VARIOUS 3D PRINTING TECHNOLOGIES, MM Science Journal 2017 (2017) 2004–2012. URL: http://www.mmscience.eu/december-2017.html#201776. doi:10.17973/MMSJ.2017_12_201776.
[45] S. Yuan, F. Shen, J. Bai, C. K. Chua, J. Wei, K. Zhou, 3D soft auxetic lattice structures fabricated by selective laser sintering: TPU powder evaluation and process optimization, Materials and Design 120 (2017) 317–327. URL: http://dx.doi.org/10.1016/j.matdes.2017.01.098. doi:10.1016/j.matdes.2017.01.098, publisher: Elsevier Ltd.
[46] C. Bonatti, D. Mohr, Mechanical performance of additively-manufactured anisotropic and isotropic smooth shell-lattice materials: Simulations & experiments, Journal of the Mechanics and Physics of Solids 122 (2019) 1–26. URL: https://www.sciencedirect.com/science/article/pii/S0022509617309614. doi:10.1016/j.jmps.2018.08.022.
[47] M. Vafaeefar, K. M. Moerman, T. J. Vaughan, LatticeWorks: An open-source MATLAB toolbox for nonuniform, gradient and multi-morphology lattice generation, and analysis, Materials & Design 250 (2025) 113564. URL: https://www.sciencedirect.com/science/article/pii/S0264127524009390. doi:10.1016/j.matdes.2024.113564.
[48] D. K. Klein, M. Fernández, R. J. Martin, P. Neff, O. Weeger, Polyconvex anisotropic hyperelasticity with neural

networks, Journal of the Mechanics and Physics of Solids 159 (2022) 104703. URL: https://linkinghub.elsevier.com/retrieve/pii/S0022509621003215. doi:10.1016/j.jmps.2021.104703.

[49] M. Flaschel, S. Kumar, L. De Lorenzis, Unsupervised discovery of interpretable hyperelastic constitutive laws, Computer Methods in Applied Mechanics and Engineering 381 (2021) 113852. URL: https://www.sciencedirect.com/science/article/pii/S0045782521001894. doi:10.1016/j.cma.2021.113852.

[50] O. Z. Tikenoğulları, A. K. Açan, E. Kuhl, H. Dal, Data-driven hyperelasticity, Part II: A canonical framework for anisotropic soft biological tissues, Journal of the Mechanics and Physics of Solids 181 (2023) 105453. URL: https://www.sciencedirect.com/science/article/pii/S0022509623002570. doi:10.1016/j.jmps.2023.105453.

[51] X. Zheng, C. , Ta-Te, J. , Xiaoyu, N. , Masanobu, , I. Watanabe, Deep-learning-based inverse design of three-dimensional architected cellular materials with the target porosity and stiffness using voxelized Voronoi lattices, Science and Technology of Advanced Materials 24 (2023) 2157682. URL: https://doi.org/10.1080/14686996.2022.2157682. doi:10.1080/14686996.2022.2157682, publisher: Taylor & Francis _eprint: https://doi.org/10.1080/14686996.2022.2157682.